Forced Shear Flow of Magnetic Bubble Arrays

R. Seshadri[a] and R. M. Westervelt

Division of Applied Science and Department of Physics, Harvard University, Cambridge, Massachusetts 02138

We present direct experimental observations of collective transport in two-dimensional magnetic bubble arrays in thin garnet films. Shear flow is produced by forcing the array to move past a flat interface; the array is strongly pinned on the other side of the interface. Time-resolved images of the dislocation dynamics that produce shear flow are obtained via Voronoi constructions.

Forced flow of two-dimensional (2D) arrays subject to a disordered external potential is common to a variety of physical phenomena: vortex arrays in type II superconductors, charge density waves, fluids in porous media, domain wall motion in random magnets, and Wigner crystals on thin He films [1,2]. Vortex arrays in high-T_c superconductors have attracted considerable interest [3] because their motion causes dissipation. Traditional thermally assisted flux flow theories [4] ignore interactions between vortices and predict thermally activated vortex motion. Melting theories [5–7] predict that the shear viscosity of the array is important even in the presence of disorder; the shear viscosity increases as the liquid transforms into a hexatic and then a hexatic glass. Theories based on spin glasses [8] predict that the array becomes glassy at high densities due to the effects of disorder, and that the shear layer thickness exceeds the translational correlation length. Direct measurements of flow patterns and defect motion are desirable to test the basic assumptions made in these theories, but this microscopic information is not available in most experiments. Numerical simulations [9] are limited by computational time for large systems.

In this Letter we present direct experimental observations of collective transport and shear flow of 2D magnetic bubble arrays in thin garnet films. We track the motion of topological defects which causes macroscopic shear flow, and present measurements of the density dependence of characteristic flow parameters. Previously we showed [10] that bubble arrays undergo a hexatic-to-liquid melting transition as a function of density, and that a small amount of substrate roughness destroys translational order so that a hexatic glass [6] is the most ordered phase. These observations are analogous to observations of stationary vortex arrays in high-T_c superconductors [11].

Magnetic bubble domains in thin garnet films have been thoroughly studied for magnetic storage and magneto-optic devices [12]. For this work we used a 7.8-μm film of Bi-substituted iron garnet ($4\pi M = 190$ G, $T_{Curie} = 170\,^\circ$C) with strong growth-induced anisotropy [13]. Details of the sample characteristics and experimental setup are given elsewhere [10,14]. Magnetic bubbles are cylindrical domains of magnetization oriented perpendic-

ular to the film with thin (~ 0.1 μm) domain walls. Individual bubbles are free to move within the film plane and interact as magnetic dipoles. Our experiments are done at room temperature within a single crystallite of a large polycrystalline array of bubbles [10]. The array density ρ is controlled by using a perpendicular dc bias magnetic field H_B opposed to the bubble magnetization to break bubbles at randomly located positions. The density ρ decreases by an order of magnitude (from 4500 to 500 mm^{-2}) as the net bias field increases from 85 to 95 Oe, while the bubble radius remains essentially constant at 3.3 μm and is uniform from bubble to bubble. A fixed superimposed perpendicular ac field H_{ac} (5 Oe rms at 40 Hz) agitates bubbles to simulate thermal motion [10]. Bubble separations (15 to 45 μm) are much larger than their radii so that the interaction between bubbles is dipolar. We observe bubbles via the Faraday effect using an optical microscope. Time-resolved digitized images are recorded on a microcomputer. Topological defects in arrays are identified using Voronoi constructions [15].

We use an experimental geometry suggested by Marchetti and Nelson [7], shown in Figs. 1(a) to 1(c). The lower part of the bubble array is strongly pinned by photolithographically defined Permalloy disks evaporated onto the garnet, shown as open circles in Fig. 1; each disk is 50 Å thick and 6 μm in radius. A flat interface separates the pinned part of the bubble array from the unpinned part, and the bubble array is continuous across the interface as shown. An in-plane force F is applied parallel to the pinning interface by linearly varying the perpendicular dc bias field using small opposed magnetic-field-gradient coils on either side of the sample. In a simple hydrodynamic model [7], bubble motion is opposed by viscous drag:

$$\mathbf{F}_{drag} = -\gamma \mathbf{v} + \eta \nabla_\perp^2 \mathbf{v}. \tag{1}$$

Here v is the average bubble velocity parallel to F, γ is the coefficient of frictional drag due to substrate roughness in the sample, and η is the shear viscosity due to bubble-bubble interactions. For moderate values of the applied force F, the pinned part of the array does not move, while the portion of the array far from the interface flows uniformly with velocity $v_{bulk} = F/\gamma$. In this model the average flow velocity increases with distance y
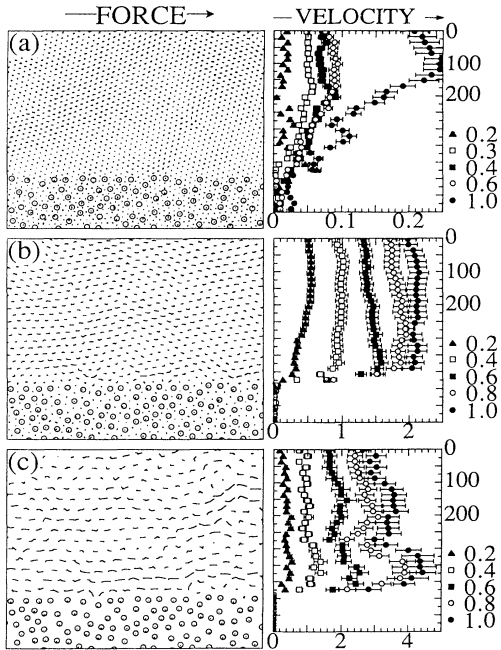
FIG. 1. Forced flow of bubble arrays: Images of size 886×675 μm^2 show flow under force F produced by gradient current $I_G = 0.6$ A at (a) hexatic glass density $\rho = 3935$ mm^{-2} over time $t = 45$ sec, (b) hexatic $\rho = 1862$ mm^{-2} over $t = 6$ sec, (c) liquid $\rho = 792$ mm^{-2} over $t = 6$ sec. Circles represent Permalloy sites. Each line represents motion of one bubble in the time period. Shown to the right of each image are measured velocity profiles at five values of F indicated by I_G in A: Plots show velocity parallel to F in μm/sec vs position from top of image in μm.

away from the interface as

$$v(y) = v_{\text{bulk}}(1 - e^{-y/\delta}) , \qquad (2)$$

where $\delta = (\eta/\gamma)^{1/2}$ is the width of the shear region.

Experiments were performed by applying a force F parallel to the interface and observing the motion of individual bubbles using a series of time-resolved digitized images. After 60 sec, the force was turned off and the array was allowed to relax to avoid building up a pressure gradient opposed to the flow. The force F is proportional to the magnetic field gradient and to the current I_G in the gradient coils: A current $I_G = 1$ A produces a gradient $dH/dx = 0.005$ Oe/μm $\pm$ 3% over 3000 μm, and a force $F = 4 \times 10^{-7}$ dyn on each bubble. We observed flows in three different areas of the sample, at 11 values of F evenly spaced between $I_G = 0$ and 1 A, for 20 values of ρ between 4500 and 750 mm^{-2} spanning the hexatic glass, hexatic, and liquid.

The left portion of Fig. 1 shows measured flows at three densities corresponding to a hexatic glass [Fig. 1(a)], a hexatic [Fig. 1(b)], and a liquid [Fig. 1(c)]. Each line represents the recorded motion of one bubble flowing in response to a force F applied parallel to the in-

terface by a current $I_G = 0.6$ A, over a time period of 45, 6, and 6 sec for Figs. 1(a), 1(b), and 1(c), respectively. To the right side of each picture we plot measured profiles of the average bubble velocity parallel to the interface for five increasing values of force. As shown, the part of the array under the pinning sites does not move appreciably, while away from the interface the unpinned array flows uniformly. In Figs. 1(a) and 1(b) bubbles move along lattice lines for short times. Over longer times the average flow is parallel to the applied force. The bulk velocity v_{bulk} increases approximately linearly with force for small forces F produced by $I_G \leq 0.4$ A for the liquid, $I_G \leq 1$ A for the hexatic, and $I_G \leq 0.6$ A for the hexatic glass. The average velocity increases from zero at the interface to a uniform value v_{bulk} well away from the interface over a shear layer of width δ which decreases with density ρ.

We find that the forced flow of magnetic bubble arrays is intimately related to the dynamics of dislocations in the array. Observations of the shear region indicate that the gliding motion of interacting dislocations leads to slip events which add to produce the macroscopic shear flow. This is illustrated in Fig. 2 by an array of density $\rho = 3459$ mm^{-2} flowing in response to a force produced by $I_G = 0.5$ A, as shown in Figs. 2(1) to 2(3). Figures 2(a) to 2(d) show the positions of dislocations at times $t = 0$, 15, 30, and 45 sec, respectively; each dislocation is shown as a fivefold (square) and sevenfold (circle) disclination pair. When the local shear stress becomes large, a slip event produced by dislocation glide allows the array to move forward, relaxing the stress locally and transferring it to other areas. The slip event shown in Fig. 2(1) is due to a dislocation pair which nucleates and separates as shown in Fig. 2(a). A bound dislocation pair is represented by two squares and two circles arranged in a quadrupole [10]. A bound pair is created in Fig. 2(a), and the dislocations separate and glide apart between Figs. 2(a) and 2(b) as indicated by arrows. One dislocation glides out of the image, and the other glides into another dislocation present in the array and annihilates as shown. The slip event in Fig. 2(2) is due to a dislocation gliding to the right between Figs. 2(b) and 2(c), as indicated by arrows. The slip event on the right-hand side of Fig. 2(3) is due to a dislocation gliding in from the right between Figs. 2(c) and 2(d) as indicated. The slip event on the left-hand side of Fig. 2(3) is due to a dislocation pair that nucleates and separates between Figs. 2(c) and 2(d).

In arrays with lower density ρ the number of dislocations present is larger, and gliding dislocations collide more often, making each slip event shorter. In Fig. 3 we illustrate three basic processes of dislocation motion and interaction observed in the shear region. Shown in Fig. 3(a) is the nucleation and ionization of a dislocation pair previously seen in Fig. 2, consistent with stress-induced pair separation in theoretical studies [16]. This nonlinear process provides free dislocations and is particularly important in the flow of the hexatic glass whose equilibrium
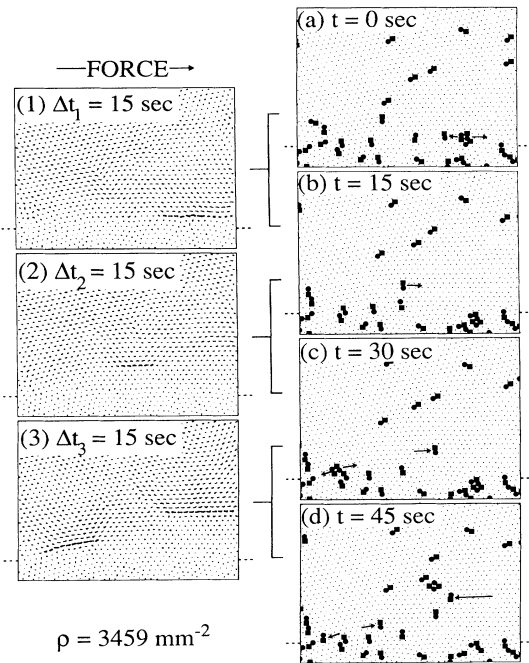
235

FIG. 2. Dislocation dynamics in shear flow: (a) to (d) Images of size 1000×740 μm^2 show dislocation motion in bubble array with $\rho = 3459$ mm^{-2} flowing under a force due to $I_G = 0.5$ A at times (a) 0 sec, (b) 15 sec, (c) 30 sec, and (d) 45 sec. Dots represent bubbles. Solid squares and circles represent bubbles with five and seven adjacent bubbles. Square-circle pairs represent dislocations with arrows indicating glide motion. (1) to (3) show flow over each 15-sec interval. Each line represents motion of one bubble in the time period. Thick lines highlight slip events. Dashed lines on either side of (a) to (d) and (1) to (3) indicate position of the pinning interface.
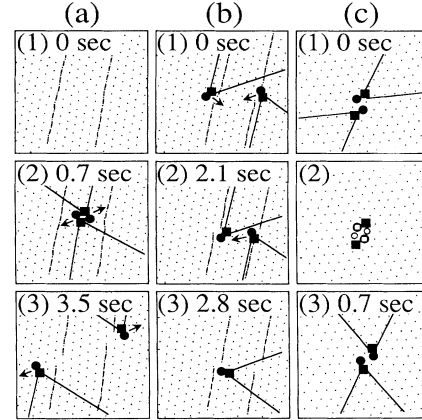

FIG. 3. Dislocation dynamics in shear region: (a) Virtual pairs nucleate and ionize. (b) Gliding dislocations combine. (c) Dislocations in vacancy pair reorient. Dots represent bubbles. Squares and circles represent bubbles with five and seven adjacent bubbles. Square-circle pairs represent dislocations with arrows indicating glide. Dashed lines highlight lattice lines. Solid lines highlight extra rows associated with dislocations.

dislocation concentration is very low. As shown in Fig. 3, when the local shear stress becomes large the defect-free hexagonal array in Fig. 3(a.1) distorts to produce a bound dislocation pair in Fig. 3(a.2). Dislocations in the shear region with glide directions parallel to the bulk flow are expected to move in the direction of their Burgers vectors in order to relax the shear stress [17]. The two dislocations in Fig. 3(a.2) glide apart in Fig. 3(a.3), shearing the array as indicated by dashed lines. Similarly, the dislocations in Figs. 3(b.1) and 3(b.2) glide along the arrows in response to the shear stress. When they collide in Fig. 3(b.3) they combine into a single dislocation with different orientation. Dislocations in the vacancy pair in Fig. 3(c.1) reorient in Fig. 3(c.3) so that their glide directions are parallel to the bulk flow, perhaps via the excitation of a pair in Fig. 3(c.2).

In Fig. 4(a) we plot the widths δ determined from fitting Eq. (2) to measured velocity profiles versus the bubble density ρ, together with measured orientational (ξ_θ) and translational (ξ_T) correlation lengths. As shown, δ increases from $\sim 1a$ in the liquid to $\sim 10a$ in

the hexatic glass; $\delta \sim \xi_T$ at high bubble densities, indicating that the bubble array does not undergo a freezing process analogous to a spin glass for which we expect $\delta \gg \xi_T$ [8]. Figure 4(b) shows the frictional drag γ due to substrate roughness measured from the linear response of v_{bulk} vs F. At small values of ρ the measured frictional drag γ is close to γ_{iso} measured for isolated bubbles (solid line), and the drag γ increases with density ρ. The inset in Fig. 4(b) shows a linear plot of the density dependence of $1/\gamma$, analogous to resistivity measured for vortex arrays in type II superconductors. We do not observe the hexatic-to-liquid transition in $1/\gamma$, and the curve extrapolates to zero when the nonequilibrium hexatic becomes a hexatic glass as the dislocation concentration decreases [14]. Figure 4(c) shows that the shear viscosity $\eta = \delta^2 \gamma$ also increases strongly with density ρ. Because shear flow is produced by dislocation glide, the shear viscosity η is inversely proportional to the dislocation concentration ρ_D and mobility B_{glide} [18], both of which are measured to decrease with increasing density ρ [10].

In the free-area model [19] the number of dislocations in an array is proportional to the average free area α_f available, which is the difference between the average area per bubble $1/\rho$ in the array and an area $1/\rho_0$, where ρ_0 is the density above which bubbles are so densely packed that dislocations are absent. When the local free area surrounding a bubble exceeds a critical value α^* it can escape from its neighbors and become part of a dislocation. A statistical distribution of free area over all bubbles [19] gives the diffusion constant for bubble motion, from which the dislocation concentration is found to be $\rho_D \propto \rho \exp[-g\alpha^* \rho_0 \rho / (\rho_0 - \rho)]$, where g is a numerical factor between $\frac{1}{2}$ and 1 to correct for overlap of free
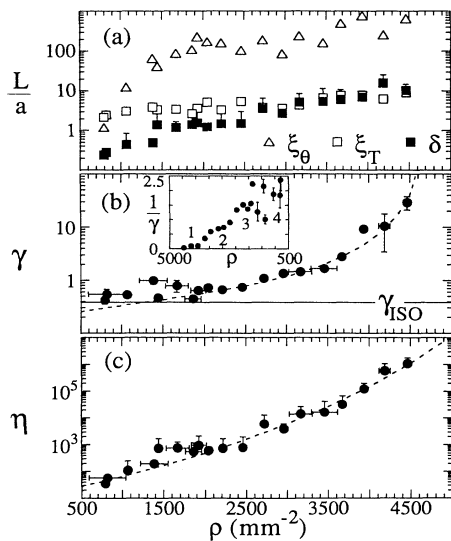
FIG. 4. (a) Measured widths δ of the shear region, and orientational (ξ_θ) and translational (ξ_T) correlation lengths of the bulk, all in units of average lattice spacing a, vs array density ρ. (b) Frictional drag γ in $A\sec/\mu m$. Solid line is γ_{iso} measured for isolated bubbles. Dashed-line fit increases as $\gamma \propto \rho e^{ga^*\rho_0/(\rho_0-\rho)}$ from γ_{iso}. Inset: A linear plot of $1/\gamma$ vs ρ. The numbers indicate the observed phase of the array: 1 = hexatic glass, 2 = nonequilibrium hexatic, 3 = equilibrium hexatic, and 4 = liquid. (c) Shear viscosity η in $A\sec\mu m$. Dashed line is a fit $\eta \propto e^{(ga^*+C_1)\rho_0\rho/(\rho_0-\rho)}$ (see text).

area. The mobility B_{glide} is given by an Arrhenius model for the diffusion of dislocations and Einstein's equation [19]: $B_{glide} \cong v(k_BT)^{-1}\rho^{-1}\exp(-E/k_BT)$, where k_BT is the thermal energy and v is the attempt frequency of dislocations gliding in the fixed ac field. The energy barrier E for a dislocation to move one step of size $\rho^{-1/2}$ increases with array density: $E/k_BT \cong C_0+C_1\rho$ so that $B_{glide} \propto \rho^{-1}\exp(-C_1\rho)$. As a result, the shear viscosity $\eta \propto (\rho_D B_{glide})^{-1}$ is given by $\eta \propto \exp[(ga^*+C_1)\rho_0\rho/(\rho_0-\rho)]$. A fit to the data in Fig. 4(c) (dashed line) gives $(ga^*+C_1)\rho_0 = 16.58$ and $r_0 = (\pi\rho_0)^{-1/2} = 5.4 \pm 0.5$ μm. The free-area model also describes bulk flow: Because the thermal energy is fixed, the diffusion constant for bubble motion is inversely proportional to the drag γ via Einstein's equation. Therefore the drag increases as $\gamma \propto \rho\exp[ga^*\rho_0/(\rho_0-\rho)]$ from γ_{iso}. The dashed line fit in Fig. 4(b) gives $r_0 = 7.6 \pm 0.7$ μm, $\gamma_{iso} = 0.20 \pm 0.16$ $A\sec/\mu m$, which is close to the measured value $\gamma_{iso} = 0.39$ $A\sec/\mu m$, and the critical size of voids necessary for bubble displacements in the bulk flow $ga^* = 163$ μm^2.

We thank Roger Belt for the samples, Steve Fortune for the Voronoi code, and Frans Spaepen, Daniel Fisher, Jed Dempsey, and especially David Nelson for helpful conversations. This work was supported in part by ONR

[a]Present address: AT&T Bell Laboratories, Murray Hill, NJ 07974.

[1] A. I. Larkin and Yu. N. Ovchinikov, Zh. Eksp. Teor. Fiz. 65, 1704 (1974); 68, 1915 (1975) [Sov. Phys. JETP 38, 854 (1974); 41, 960 (1975)].

[2] D. S. Fisher, in Nonlinearity in Condensed Matter, edited by A. R. Bishop, D. K. Campbell, P. Kumar, and S. E. Trullinger (Springer-Verlag, New York, 1987).

[3] D. R. Nelson and D. S. Fisher, in Phenomenology and Applications of High Temperature Superconductors, edited by K. Bedell, M. Inui, D. Meltzer, J. R. Schrieffer, and S. Doniach (Addison-Wesley, New York, 1991).

[4] P. H. Kes, J. Aarts, J. van den Berg, and J. A. Mydosh, Supercond. Sci. Technol. 1, 241 (1989).

[5] B. I. Halperin and D. R. Nelson, Phys. Rev. Lett. 41, 121 (1978); D. S. Fisher, Phys. Rev. B 22, 1190 (1980); D. R. Nelson, in Phase Transitions and Critical Phenomena, edited by C. Domb and J. L. Lebowitz (Academic, London, 1983), Vol. 7.

[6] E. M. Chudnovsky, Phys. Rev. B 40, 11355 (1989); J. P. Bouchaud, M. Mezard, and J. S. Yedidia, Phys. Rev. Lett. 67, 3840 (1991).

[7] M. C. Marchetti and D. R. Nelson, Phys. Rev. B 42, 9938 (1990); Physica (Amsterdam) 174C, 40 (1991).

[8] M. P. A. Fisher, T. A. Tokuyasu, and A. P. Young, Phys. Rev. Lett. 66, 2931 (1991); D. S. Fisher, M. P. A. Fisher, and D. Huse, Phys. Rev. B 43, 130 (1991).

[9] D. Frenkel and J. P. McTauge, Phys. Rev. Lett. 42, 1632 (1979); A. Shi and A. J. Berlinsky, Phys. Rev. Lett. 67, 1926 (1991).

[10] R. Seshadri and R. M. Westervelt, Phys. Rev. Lett. 66, 2774 (1991); Phys. Rev. B 46, 5142 (1992); 46, 5150 (1992).

[11] C. A. Murray, P. L. Gammel, D. J. Bishop, D. B. Mitzi, and A. Kapitulnik, Phys. Rev. Lett. 64, 2312 (1990); D. G. Grier, C. A. Murray, C. A. Bolle, P. L. Gammel, D. J. Bishop, D. B. Mitzi, and A. Kapitulnik, Phys. Rev. Lett. 66, 2270 (1991).

[12] A. H. Eschenfelder, Magnetic Bubble Technology (Springer-Verlag, New York, 1981); A. P. Malozemoff and J. C. Slonczweski, Magnetic Domain Walls in Bubble Materials (Academic, New York, 1979).

[13] R. F. Belt and J. B. Ings, SPIE J. 753, 142 (1987).

[14] R. Seshadri and R. M. Westervelt (to be published).

[15] S. Fortune, Algorithmica 2, 153 (1987).

[16] R. Bruinsma, B. I. Halperin, and A. Zippelius, Phys. Rev. B 25, 579 (1982).

[17] M. Peach and J. S. Koehler, Phys. Rev. 80, 436 (1950).

[18] J. P. Hirth and J. Lothe, Theory of Dislocations (Wiley, New York, 1982); D. Hull and D. J. Bacon, Introduction to Dislocations (Pergamon, New York, 1984).

[19] M. H. Cohen and D. Turnbull, J. Chem. Phys. 31, 1164 (1959); F. Spaepen, in Physics of Defects, edited by R. Balian et al. (North-Holland, Amsterdam, 1981).